Qualitative and quantitative evaluation of *in vivo* SD-OCT measurement of rat brain

YIJING XIE,[1,2,*] LAURA-ADELA HARSAN,[3,4,5] THOMAS BIENERT,[3] ROBERT D. KIRCH,[1] DOMINIK VON ELVERFELDT,[3] AND ULRICH G. HOFMANN[1,6]

[1]*Section of Neuroelectronic Systems, Department of General Neurosurgery, Medical Center University of Freiburg, Engesserstraße 4, 79108 Freiburg, Germany*
[2]*Translational Imaging Group, Centre for Medical Image Computing, Department of Medical Physics and Biomedical Engineering, University College London, WC1E 6BT London, UK*
[3]*Department of Diagnostic Radiology, Medical Center University of Freiburg, Hugstetter Straße 55, 79106 Freiburg, Germany*
[4]*Laboratory of Engineering, Informatics and Imaging (ICube), Integrative Multimodal Imaging in Healthcare (IMIS), UMR 7357, University of Strasbourg, 4 Rue Kirschleger, 67000 Strasbourg, France*
[5]*Department of Biophysics and Nuclear Medicine, Hautepierre Hospital, University Hospitals of Strasbourg, 1, Avenue Molière, 67098 Strasbourg Cedex, France*
[6]*Freiburg Institute for Advanced Studies (FRIAS), University of Freiburg and University of Strasbourg Institute for Advanced Study (USIAS), Strasbourg, France*
[*]*y.xie@ucl.ac.uk*

Abstract: OCT has been demonstrated as an efficient imaging modality in various biomedical and clinical applications. However, there is a missing link with respect to the source of contrast between OCT and other modern imaging modalities, no quantitative comparison has been demonstrated between them, yet. We evaluated, to our knowledge, for the first time *in vivo* OCT measurement of rat brain with our previously proposed forward imaging method by both qualitatively and quantitatively correlating OCT with the corresponding T1-weighted and T2-weighted magnetic resonance images, fiber density map (FDM), and two types of histology staining (cresyl violet and acetylcholinesterase AchE), respectively. Brain anatomical structures were identified and compared across OCT, MRI and histology imaging modalities. Noticeable resemblances corresponding to certain anatomical structures were found between OCT and other image profiles. Correlation was quantitatively assessed by estimating correlation coefficient (R) and mutual information (MI). Results show that the 1-D OCT measurements in regards to the intensity profile and estimated attenuation factor, do not have profound linear correlation with the other image modalities suggested from correlation coefficient estimation. However, findings in mutual information analysis demonstrate that there are markedly high MI values in OCT-MRI signals.

© 2017 Optical Society of America

References and links

1. C. K. Hitzenberger, "Optical measurement of the axial eye length by laser doppler interferometry," Invest Ophthalmol Vis Sci **32**, 616–624 (1991).
2. D. Huang, E. Swanson, C. Lin, J. Schuman, W. Stinson, W. Chang, M. Hee, T. Flotte, K. Gregory, C. Puliafito, and a. et, "Optical coherence tomography," Science **254**(5035), 1178–1181 (1991).
3. M. Wojtkowski, V. Srinivasan, T. Ko, J. Fujimoto, A. Kowalczyk, and J. Duker, "Ultrahigh-resolution, high-speed, fourier domain optical coherence tomography and methods for dispersion compensation," Opt. Express **12**(11), 2404–2422 (2004).
4. D.-h. Choi, H. Hiro-Oka, K. Shimizu, and K. Ohbayashi, "Spectral domain optical coherence tomography of multi-MHz A-scan rates at 1310 nm range and real-time 4D-display up to 41 volumes/second," Biomed. Opt. Express **3**(12), 3067–3086 (2012).
5. J. G. Fujimoto, "Optical coherence tomography for ultrahigh resolution in vivo imaging," Nat Biotech **21**(11), 1361–1367 (2003).

6. B. Potsaid, I. Gorczynska, V. J. Srinivasan, Y. Chen, J. Jiang, A. Cable, and J. G. Fujimoto, "Ultrahigh speed spectral / fourierdomain oct ophthalmic imaging at 70,000 to 312,500 axial scans per second," Opt. Express **16**(19), 15149–15169 (2008).

7. G. J. Tearney, M. E. Brezinski, B. E. Bouma, S. A. Boppart, C. Pitris, J. F. Southern, and J. G. Fujimoto, "In vivo endoscopic optical biopsy with optical coherence tomography," Science **276**(5321), 2037–2039 (1997).

8. T.-H. Tsai, B. Potsaid, Y. K. Tao, V. Jayaraman, J. Jiang, P. J. S. Heim, M. F. Kraus, C. Zhou, J. Hornegger, H. Mashimo, A. E. Cable, and J. G. Fujimoto, "Ultrahigh speed endoscopic optical coherence tomography using micromotor imaging catheter and vcsel technology," Biomed. Opt. Express **4**(7), 1119–1132 (2013).

9. Y. Xie, T. Bonin, S. Löffler, G. Hüttmann, V. Tronnier, and U. G. Hofmann, "Coronal in vivo forward-imaging of rat brain morphology with an ultra-small optical coherence tomography fiber probe," Phys. Med. Biol. **58**(3), 555–568 (2013).

10. Y. Xie, N. Martini, C. Hassler, R. Kirch, A. Seifert, T. Stieglitz, and U. G. Hofmann, "In vivo monitoring of glial scar proliferation on chronically implanted neural electrodes by fiber optical coherence tomography," Front Neuroeng **7**(34) (2014).

11. S. W. Jeon, M. A. Shure, K. B. Baker, D. Huang, A. M. Rollins, A. Chahlavi, and A. R. Rezai, "A feasibility study of optical coherence tomography for guiding deep brain probes," J. Neurosci. Methods **154**(1-2), 96 – 101 (2006).

12. M. Gloesmann, B. Hermann, C. Schubert, H. Sattmann, P. K. Ahnelt, and W. Drexler, "Histologic correlation of pig retina radial stratification with ultrahigh-resolution optical coherence tomography," Invest. Ophthalmol. Vis. Sci. **44**(4), 1696–1703 (2003).

13. R. Kuranov, V. Sapozhnikova, D. Prough, I. Cicenaite, and R. Esenaliev, "Correlation between optical coherence tomography images and histology of pigskin," Appl. Opt. **46**(10), 1782–1786 (2007).

14. R. John, S. G. Adie, E. J. Chaney, M. Marjanovic, K. V. Tangella, and S. A. Boppart, "Three-dimensional optical coherence tomography for optical biopsy of lymph nodes and assessment of metastatic disease," Ann Surg Oncol **20**(11), 3685–3693 (2013).

15. C. I. Unglert, W. C. Warger, J. Hostens, E. Namati, R. Birngruber, B. E. Bouma, and G. J. Tearney, "Validation of two-dimensional and three-dimensional measurements of subpleural alveolar size parameters by optical coherence tomography." J. Biomed. Opt. **17**(12), 126015 (2012).

16. I. Gudmundsdottir, P. Adamson, C. Gray, J. C. Spratt, M. W. Behan, P. Henriksen, D. E. Newby, N. Mills, N. G. Uren, and N. L. Cruden, "Optical coherence tomography versus intravascular ultrasound to evaluate stent implantation in patients with calcific coronary artery disease," Open Heart **2**(1) (2015).

17. M. A. Jacobs, J. P. Windham, H. Soltanian-Zadeh, D. J. Peck, and R. A. Knight, "Registration and warping of magnetic resonance images to histological sections," Med. Phys. **26**(8), 1568–1578 (1999).

18. G. Paxinos and C. Watson, *The Rat Brain in Stereotaxic Coordinates* (Academic, 2005), fifth edition ed.

19. Z. Eaton-Rosen, A. Melbourne, E. Orasanu, M. J. Cardoso, M. Modat, A. Bainbridge, G. S. Kendall, N. J. Robertson, N. Marlow, and S. Ourselin, "Longitudinal measurement of the developing grey matter in preterm subjects using multi-modal MRI," NeuroImage **111**, 580–589 (2015).

20. W. Jensen, U. G. Hofmann, and K. Yoshida, "Assessment of subdural insertion force of single-tine microelectrodes in rat cerebral cortex," in Proceedings of the 25th Annual International Conference of the IEEE, vol. 3 (2003), pp. 2168–2171.

21. D. Paul, M. Zaitsev, L. Harsan, A. Kurutsch, D. N. Splitthoff, F. Hennel, M. Choli, and D. von Elverfeldt, "Implementation and application of PSF-based EPI distortion correction to high field animal imaging." Int. J. Biomed. Imaging **2009**, 946271 (2009).

22. L.-A. Harsan, D. Paul, S. Schnell, B. W. Kreher, J. Hennig, J. F. Staiger, and D. von Elverfeldt, "In vivo diffusion tensor magnetic resonance imaging and fiber tracking of the mouse brain." NMR Biomed **23**(7), 884–96 (2010).

23. M. Reisert, I. Mader, C. Anastasopoulos, M. Weigel, S. Schnell, and V. Kiselev, "Global fiber reconstruction becomes practical," NeuroImage **54**(2), 955–962 (2011).

24. L.-A. Harsan, C. Dávidb, M. Reiserta, S. Schnella, J. Henniga, D. von Elverfeldta, and J. F. Staigerd, "Mapping remodeling of thalamocortical projections in the living reeler mouse brain by diffusion tractography." Proceedings of the National Academy of Sciences **110**(19), E1797–E1806 (2013).

25. C. S. Myers and L. R. Rabiner, "A comparative study of several dynamic time-warping algorithms for connected-word recognition," Bell System Technical Journal **60**(7), 1389–1409 (1981).

26. E. Keogh and C. A. Ratanamahatana, "Exact indexing of dynamic time warping," Knowl. Inf. Syst. **7**(3), 358–386 (2005).

27. Y.-S. Jeong, M. K. Jeong, and O. A. Omitaomu, "Weighted dynamic time warping for time series classification," Pattern. Recogn. **44**(9), 2231 – 2240 (2011).

28. K. Pearson, "Notes on regression and inheritance in the case of two parents," in Proceedings of the Royal Society of London, vol. 58 (1895), pp. 240–242.

29. A. L. Edwards, *The Correlation Coefficient* (W.H. Freeman & Co Ltd, 1976).

30. M. Krzywinski and N. Altman, "Points of significance: Visualizing samples with box plots," Nat. Meth. **11**(2), 119–120 (2014).

31. T. M. Cover, and J. A. Thomas, *Elements of information theory* John Wiley & Sons, 2012.

32. F. Maes, A. Collignon, D. Vandermeulen, G. Marchal, and P. Suetens "Multimodality image registration by maximization of mutual information," IEEE Trans. Med. Imaging **16**(2), 187–198 (1997).

33. J. T. Bushberg, J. A. Seibert, J. Edwin M. Leidholdt, and J. M. Boone, *The Essential Physics of Medical Imaging* (Lippincott Williams & Wilkins, 2002).
34. W. D. Rooney, G. Johnson, X. Li, E. R. Cohen, S.-G. Kim, K. Ugurbil, and C. S. Springer, "Magnetic field and tissue dependencies of human brain longitudinal 1H2O relaxation in vivo," Magn. Reson. Med. **57**(2), 308–318 (2007).
35. M. Khalil, C. Langkammer, S. Ropele, K. Petrovic, M. Wallner-Blazek, M. Loitfelder, M. Jehna, G. Bachmaier, R. Schmidt, C. Enzinger, S. Fuchs, and F. Fazekas, "Determinants of brain iron in multiple sclerosis: A quantitative 3T MRI study," Neurology **77**(18), 1691–1697 (2011).
36. I. J. Bigio and S. Fantini, *Quantitative biomedical optics: theory, methods, and applications* (Cambridge University, 2016).
37. W. Drexler, Y. Chen, A. Aguirre, B. Považay, A. Unterhuber, and J. G. Fujimoto, *Optical coherence tomography: Technology and applications for neuroimaging* (Springer, 2008), chap. 8: Ultrahigh resolution optical coherence tomography, pp. 239–279.
38. M. Mulisch and U. Welsch, eds., *Romeis Mikroskopische Technik*, 18th ed. (Spektrum Akademischer Verlag, 2010).
39. C. A. Paul, B. Beltz, and J. Berger-Sweeney, "Staining for acetylcholinesterase in brain sections," Cold Spring Harbor Protocols **2010**, 8 (2010).
40. J. V. Rosenfeld, "Minimally invasive neurosurgery," Aust N Z J Surg **66**(8), 553–559 (1996).
41. L. T. Holly, J. D. Schwender, D. P. Rouben, and K. T. Foley, "Minimally invasive transforaminal lumbar interbody fusion: indications, technique, and complications," Neurosurg. Focus **20**(3), 1–5 (2006).
42. S. Hemm and K. Wårdell, "Stereotactic implantation of deep brain stimulation electrodes: a review of technical systems, methods and emerging tools," Med. Biol. Eng. Comput. **48**(7), 611–624 (2010).
43. R. Sparks, G. Zombori, R. Rodionov, M. Nowell, S. B. Vos, M. A. Zuluaga, B. Diehl, T. Wehner, A. Miserocchi, A. W. McEvoy, J. S. Duncan, and S. Ourselin, "Automated multiple trajectory planning algorithm for the placement of stereo-electroencephalography (SEEG) electrodes in epilepsy treatment," Int. J. Comput. Assist. Radiol. Surg. pp. 1–14 (2016).
44. J. D. Johansson and K. Wårdell, "Intracerebral quantitative chromophore estimation from reflectance spectra captured during deep brain stimulation implantation," J. Biophotonics **6**(5), 435–445 (2013).
45. A. I. Kholodnykh, I. Y. Petrova, M. Motamedi, and R. O. Esenaliev, "Accurate measurement of total attenuation coefficient of thin tissue with optical coherence tomography," IEEE J. Sel. Top. Quantum Electron. **9**(2), 210–221 (2003).
46. T. G. van Leeuwen, D. J. Faber, and M. C. Aalders, "Measurement of the axial point spread function in scattering media using single-mode fiber-based optical coherence tomography," IEEE J. Sel. Top. Quantum Electron. **9**(2), 227–233 (2003).
47. G. van Soest, T. Goderie, E. Regar, S. Koljenović, G. L. J. H. van Leenders, N. Gonzalo, S. van Noorden, T. Okamura, B. E. Bouma, G. J. Tearney, J. W. Oosterhuis, P. W. Serruys, and A. F. W. van der Steen, "Atherosclerotic tissue characterization in vivo by optical coherence tomography attenuation imaging," J. Biomed. Opt. **15**(1), 011105 (2010).
48. L. Scolaro, R. A. McLaughlin, B. R. Klyen, B. A. Wood, P. D. Robbins, C. M. Saunders, S. L. Jacques, and D. D. Sampson, "Parametric imaging of the local attenuation coefficient in human axillary lymph nodes assessed using optical coherence tomography," Biomed. Opt. Express **3**(2), 366–379 (2012).

1. Introduction

Optical coherence tomography (OCT) is a non-ionising optical imaging modality introduced in the early 90's [1, 2]. It utilises optical scattering properties of the tissue to generate an image where the contrast comes from differences in the optical reflectivity and backscattering of the tissue. Featuring a high imaging resolution of about 2 μm [3], and fast imaging speed up to 10 millions axial scans per second [4], OCT has been demonstrated as an efficient imaging modality in various biomedical and clinical applications, such as retinal imaging for diagnostic purpose [5, 6]. When integrated with a glass fiber catheter, it allows to perform minimally invasive endoscopic interventions of inner organs [7–10]. In particular, the fiber-based OCT has the potential to facilitate distinction of brain anatomical structures for real-time minimally-invasive surgical guidance [9, 11].

The evaluation is often done by qualitatively comparing OCT images with the corresponding tissue histology or an atlas [12–14]. There is a missing link between OCT and the other imaging modalities such as magnetic resonance imaging (MRI) or computed tomography (CT) with respect to the fundamental sources and relation of respective image contrast. Unglert et al. have validated OCT measurements of alveolar size by correlating them with CT measurements quan-

titatively [15]. However, this validation process was conducted on formaldehyde fixed swine lung specimens, thus both OCT and CT measurements were performed *ex vivo*. Gudmunds-dottir et al. investigated the linear correlation between frequency domain optical coherence tomography (FD-OCT) and intravascular ultrasound (IVUS) in patients with calcific coronary artery disease [16]. The demand for quantitatively evaluation of *in vivo* OCT measurements by correlating with other well-established imaging exists.

The goal of this study was to evaluate *in vivo* OCT measurement of rat brain with our previously proposed forward imaging method [9] by qualitatively and quantitatively correlating it with the corresponding T1 and T2-weighted magnetic resonance images (MRI), fiber density map (FDM), and two types of tissue staining (cresyl violet and acetylcholinesterase), respectively [17–19]. Brain anatomical structures were distinguished in OCT measurements, and correlated between OCT, MRI and histology images. For quantification, we first used resampling to equalize the sample length of all signals. Direct comparison were performed on the consolidated signals to find any resemblances between image profiles. We used dynamic time warping (DTW) to estimate the cost of align the two signals. Correlation coefficient (R) was calculated to assess linear correlation of each pair's correlation degree. Mutual information (MI) was determined to evaluate information shared between cross-modality signals. This is, to the extent of our knowledge, the first report to both qualitatively and quantitatively correlate OCT measurements with other modern imaging modalities. Results indicate the reported OCT forward imaging method is an efficient imaging modality for *in vivo* brain measurement of living animals, and could be potentially integrated to minimally-invasive neurointervention as guidance.

2. Materials and methods

2.1. OCT signal acquisition

The *in vivo* optical coherence tomography (OCT) measurements of rat brain were performed with a fiber-based Spectral-Domain OCT (SDOCT) system utilising a super-luminescent diode (SLD) with center wavelength at 840 nm as a light source. The measured axial resolution of the system is 14.5 μm in air. The SDOCT system is connected to an ultra-thin single mode glass fiber based catheter, of which the outer diameter is 125 μm, enabling minimally invasive forward imaging within the brain of living animals [9].

In total, ten animals were included in OCT measurements. All animal experiments conducted in this study were performed with approval from the locally responsible Animal Welfare Committe with the Regierungspräsidium Freiburg in accordance with the guidelines of the European Union Directive 2010/63/UE. The animal model chosen consists of adult female Sprague Dawley rats (Charles River, Germany), weighing 280-320 g. The rats were initially anaesthetized by a cocktail of 100 mg/kg ketamine and 5 mg/kg xylazine, administered by intraperitoneal (i.p.) injection, and were given acepromazin on the scalp prior to the operation for pain management. The body temperature was maintained at 37 °C by a circulating water-bath heating pad. The rat was fixed into a stereotactic frame with a pair of ear bars and a bite clip. A burr hole ($\varnothing$1 mm) was drilled through the skull by using a cordless handheld microdrill. The dura mater was removed with fine-tipped tweezers and the pia mater was perforated with a 29 G hypodermic needle, before the fiber probe was inserted into the brain. Thereby, the dimpling effect in brain tissue during the probe insertion was minimized [20]. During the experiment, the rat's anaesthesia status was maintained by giving 30% of the initial anaesthesia dose i.p. when the rat showed a toe-twitch reflex. Physiological saline and glucose was injected subcutaneously in order to supplement the body fluid.

The fiber catheter was advanced into the brain along a ventral-dorsal orientated trajectory stepwisely with an increment of 0.2 mm. At each depth position along the trajectory, an OCT A-scan signal was recorded for about 30 s. Then the A-scan signal from each depth was plotted as a function of the forward distance, was averaged and vertically aligned to construct a gray
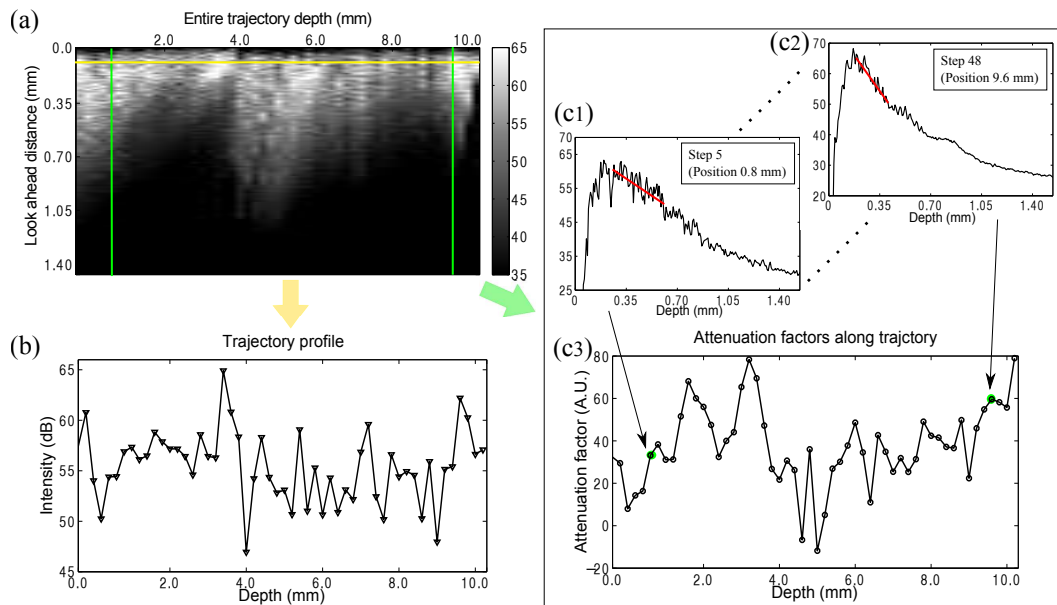
Fig. 1. An illustration of trajectory profiles extracted from OCT data, displaying intensity and attenuation data. (a) A gray scale image of a sample trajectory reconstructed from 51 vertically aligned A-scan signals taken from 51 measuring steps of along this trajectory. (b) The line profile signal of the OCT image is obtained at the position indicated by a yellow line in (a). The attenuation factor of brain tissue is calculated from the A-scan signal at each depth position in the trajectory, (c1) shows the A-scan plot from position at 0.8 mm (marked by the left green line in (a)). (c2) shows the A-scan plot from position at 9.6 mm (marked by the right green line in (a)). The red lines in these two A-scan plots demonstrate the linear fit by which the attenuation factor is extracted. The overall attenuation profile of the trajectory is shown in (c3).

scale image of this trajectory, shown in Fig. 1(a). Two types of quantitative measures derived from OCT A-scans were used to correlate with the other image modalities: (i) Trajectory profile which was taken from the reconstructed OCT image at the horizontal position 0.1 mm ahead of the probe indicated by a yellow line, shown in Fig. 1(b). This 0.1 mm depth position was determined empirically as we found that OCT A-scans amplitude reached the maximum value around this depth in homogeneous optical phantom. (ii) Attenuation coefficient data [Fig. 1(c3)] of which each data point was extracted from the linear fit of the corresponding A-scan plot [Figs. 1(c1) and 1c2)] along the trajectory. The penetration depth of brain tissue at the utilized 840 nm light source is around 1 mm [11], thus we applied fitting on 0.3 mm length of A-scan signal to get the attenuation factor.

2.2. Signal acquisition with MRI and DT-MRI

The magnetic resonance (MR) image acquisition was conducted with a 9.4 T small-bore animal scanner (Bruker BioSpec 94/20, Ettlingen, Germany) equipped with a BGA12S gradient system capable of 675 mT/m. For imaging rat brain, a transmit 1H quadrature birdcage resonator with an inner diameter of 72 mm was used for radio frequency excitation and a 4-channel phased array head coil was used as a receiver (Bruker BioSpin, Ettlingen, Germany) [21,22] [Fig. 2(c)]. Six from the ten animals that were measured with OCT, were further investigated with MRI scan. All animal experiments performed in the MRI study were approved by regional ethic
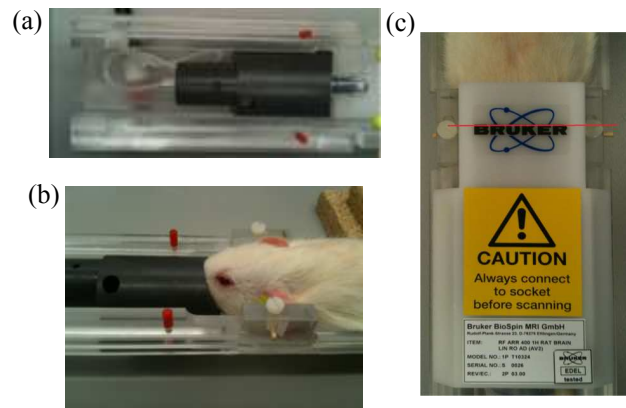
Fig. 2. Experimental setup of animal MRI measurement. (a) A MRI-adapted stereotaxic frame for fixation and ventilation tubing for anaesthesia. (b) An illustration of animal placement in the frame. (c) This picture shows the RF coil used in the measurement. The red line indicates the center position of the MR scan.

committee (approval G-13/02), and were in accordance with the guidelines of European Communities Council. Animals, of which the type, age and weight are the same as in the OCT study, were anaesthetised using an isofluran-oxygen mixture (3% isofluran for induction, 1.6 Vol% isofluran for maintenance). A MRT-adapted stereotaxic frame was used to fix the animal head, shown in Figs. 2(a) and 2(b). Heart rate, respiration, and body temperature of the animal were monitored through the whole measurement. An external heating bath pad was used to maintain the body temperature at 37 °C.

A T2-weighted RARE (Rapid Imaging with Refocused Echoes) sequence was achieved by consecutively acquiring 45 axial slices of 600 μm thickness in 29 min, which covered the whole rat brain volume. Brain coronal images were obtained with an in-plane resolution of 90 x 90 μm (matrix 256 x 188 pixel and a field of view FOV = 23 x 17 mm); repetition time (TR) of 7000 ms, echo time (TE) of 40 ms and a RARE factor of 4, for 4 averages to enhance the signal-to-noise ratio (SNR). DT-MRI data were acquired in axial 700 μm thickness slices with the same orientation as for the previous T2-weighted scans, using a 4-shots diffusion tensor echo-planar imaging (DT-EPI) weighting method. In total 40 axial slices were acquired in 99 min to cover the whole rat brain volume. Slices were acquired with a TR of 11250 ms, and a TE of 24.5 ms. Time (Δ) between the application of diffusion gradient pulses, 14 ms; diffusion gradient duration (δ), 4 ms. The acquisition protocol included the use of 30 gradient diffusion directions (Jones 30 encoding scheme), using a b-factor of 1000 s/mm^2. Four averages were used to increase the SNR. The native spatial resolution of the acquired q-space data is 202 x 202 μm at FOV of 23 x 17 mm with an acquisition matrix of 114 x 84 pixel. To explore the ensemble of living rat brain fiber pathways we adopted a 3D global fiber tracking approach that processes DTI data [23, 24]. Using the global rat brain fiber tracking data we further computed high resolution fiber density maps. The source of contrast in presented images is therefore based on the density of fibers generated during the global tracking optimisation, and passing the image voxel at specific spatial coordinates. The reconstructed high resolution fiber density maps (FDMs) have a x-y resolution of 25.2 x 25.3 μm, and were obtained in 87.5 μm slice thickness. The DTI parameter we used to compare against OCT data (both intensity profile and attenuation profile) was the intensity profile of the reconstructed FDMs.

2.3. Brain histology

For qualitative correlation, histology were performed to the rats that were examined with both MRI and OCT. The rat brains were removed right after decapitation, fixed with 4% paraformaldehyde (PFA) in phosphate-buffered saline (PBS). 20 μm thick coronal slices were obtained and prepared with Nissl staining. The microscopic imaging were captured at a scanning resolution of 4000 dpi by using a histology slide scanner (Nikon Super Coolscan LS 5000) and Vuescan scanner software.

The rat brain histology images we employed to obtain statistical assessment were taken from the widely used rat brain atlas [18]. Both cresyl violet and acetylcholinesterase (AChE) stained histology images were used for the validation. In brief, cresyl violet stains cell core and Nissl substance in dark violet, while acetylcholinesterase stains axons and cell bodies containing acetylcholine. The staining protocol were previously described by Paxinos et al. [18]. The image resolution is about 15.8 μm per pixel.

2.4. Qualitative correlation

OCT intensity profile data and attenuation coefficient data were correlated with the corresponding MRI images and histological microscopic images that were obtained from the same animal. Brain anatomical structures were identified in the OCT signals by comparing with MRI and histological images.

2.5. Quantitative correlation

Measured MRI data (T1, T2, and FDM) from one animal were utilised as the standard MRI, whilst histology images extracted from a published rat brain atlas were employed as the standard histology data [18]. The standard MRI and histology data were compared with the OCT data that were obtained from all ten animals. Coronal MRI and histological images, with the same anterior-posterior (AP) coordinate as OCT data were selected and extracted from the MRI whole brain image set and the 'rat brain atlas' sections, respectively [Fig. 3]. Then the intensity profile of the measuring trajectory where the OCT data was obtained, was extracted from each image modality. In Fig. 3, the trajectory is indicated by the red line in the image, and its corresponding profile plot is shown besides. For validation, the profile data from each image modality was used to correlate with the OCT profile data and attenuation data.

Since the OCT data were acquired with a step size of 0.2 mm yielding a signal length of approximately 50 data points while the profile signal of FDM or histological images are about of 600 data points, a preprocessing procedure including interpolation of OCT data and resample of the other profiles (FDM, histological images) was implemented to compensate the undesirable large difference in data length. We chose spline interpolation which uses low-degree polynomials in each of the intervals to increase OCT signal data points to five times more than the original signal, resulting a signals length of about 300. Then a resampling process was applied to MRI and histological signals to equalise the length of the profile signals.

2.5.1. Dynamic time warping

The consolidated signals, of which the length was equalized and the amplitude was normalized, were then warped and aligned by applying dynamic time warping (DTW). DTW determines the similarity of two time sequences which share some common waveform patterns though having different duration. It calculates the optimal alignment between two time series by identifying the optimal warping path in the distance matrix calculated under certain constrains [25–27]. DTW was used to determine the cost of aligning OCT signal with the line profile signal extracted from other imaging modalities (T1 and T2-weighted MR images, fiber density maps, histology images) for three purposes: (i) correcting distortions in the OCT data acquisition due to the
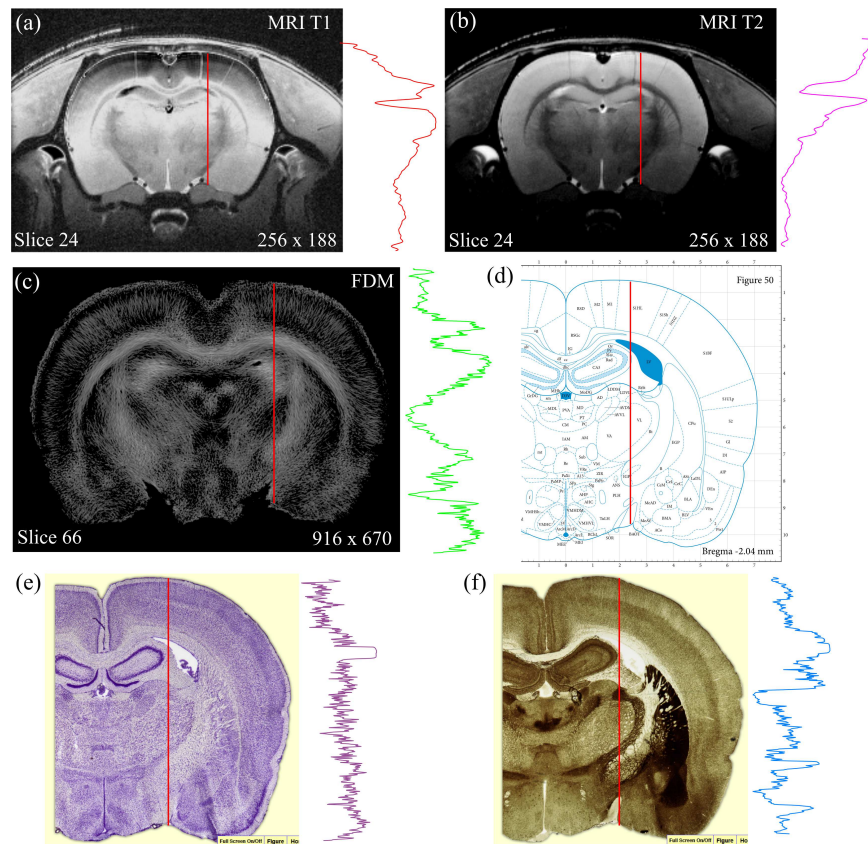
Fig. 3. A collage of selected images from MRI measurement and histological staining, and the profile data from trajectories indicated with the red line. All images (T1-weighted (a), T2-weighted (b), DTI fiber density map (c), cresyl violet staining (e), and acetyl-cholinesterase staining (f)) are with the same anterior-posterior coordinate Bregma - 2.00 mm, trajectories are located at medial-lateral - 2.50 mm. Panel (d) is the atlas sketch illustrating the anatomic structures lying on the trajectory path.

uniformity of the fiber translation, (ii) correcting distortions in the histological preparation due to the fact that the dehydration and fixation processes could deform the brain structures.

2.5.2. Correlation coefficient

For each compared signal pair, we employed Pearson's correlation coefficient to estimate the degree of linear dependency (correlation degree, R) between the two samples [15, 28, 29]. The absolute value of the sample correlation coefficient R ($R \leq 1$) of each signal pair was calculated in Matlab. Box plot (Spear style) was used to depict the statistic distribution of the determined correlation coefficient of the paired signal from six representative trajectories [30].

2.5.3. Mutual information

Mutual information (MI) is an entropy based measure that determines the statistical dependancy between two random variables [31]. It has been implemented in cross-modality image registration by determining the joint histogram of two images [32]. Because the nature of the image intensities and the relationship between the grey-values in the different modalities do not play an role in the MI conducted correlation, MI is thus a robust and efficient method to compare

signals from two different imaging modalities which present in our study. The mutual information $I(A, B)$ of two variables, A and B, is related to entropy and is calculated by the following equation

$$I(A, B) = H(A) + H(B) - H(A, B) \tag{1}$$

where $H(A)$ and $H(B)$ are the entropy of A and B, respectively. $H(A, B)$ is the joint entropy of A and B. The higher MI value means that the compared two variables are more statistically dependant. In this study, MI of two signals from their respective imaging modality is determined without applying DTW to the signals.

3. Results

3.1. Qualitative correlation

The OCT intensity profile and attenuation coefficient data were compared with T2-weighted MR images and histological images with respect to the identified anatomical structures. Two representative illustrations of the correlation of anatomical structures are shown in Fig. 4. Two dimensional grayscale OCT images were reconstructed from the sequentially acquired A-scans during translating the OCT fiber probe along a trajectory into brain, shown in Figs. 4 (a4) left and (b4) left. Both of the OCT intensity profiles and the attenuation signals presented prominent peak values corresponding to corpus callosum, superior colliculus, optic tracts, as well as cerebral peduncle which all belong to brain white matter that basically compose of neural fibers (indicated by black dotted lines). These structures revealed in OCT signals were also distinguishable in MRI and histological images. Interestingly, a high contrast in hippocampus region was only revealed in OCT attenuation signals, tentatively caused by the backscattering from multiple hippocampal layers.

3.2. Quantitative correlation of the compared signal pairs

In this study, we evaluated *in vivo* OCT measurement of rat brain by correlating the attenuation factor and intensity profiles extracted from OCT measurements on the same trajectory with profiles from T1 and T2-weighted MR images, FDM, and histological images. In total, there were 10 types of signal pairs analysed in this work, which are T1, T2, FDM, cresyl violet, and AChE correlated with OCT profile data or OCT attenuation data, respectively. We investigated the correlation degree of signal pairs from six different trajectories: AP - 5.40 mm, ML - 2.00 mm; AP - 4.70 mm, ML - 3.00 mm; AP - 4.20 mm, ML - 2.60 mm; AP - 3.50 mm, ML - 2.80 mm; AP - 2.00 mm, ML - 2.50 mm; AP - 1.00 mm, ML - 3.00 mm (all AP positions were referred to Bregma). Raw image profiles of two representative brain trajectories are shown in Fig. 5, of which the signal length is unequal due to different sampling rate or spatial resolution of respective imaging modalities. In order to align and compare signals from various imaging modalities, we applied resampling to equalize the signal length and normalization to unify the signal amplitude. The consolidated data are aligned and shown in Fig. 6. We found in trajectory A, the OCT signals presented two prominent peaks locating at trajectory depth of 2.3 mm and 3.9 mm respectively, where the anatomical structures corpus callosum and superior colliculus are. These two structures were also notably revealed in T1, FDM and AchE profiles, demonstrating resemblances between OCT signals and these image profiles, indicated by arrows in Figs. 6(a) and 6(b). Similarly, in trajectory B correspondences were identified in several depth positions across different image modalities which are indicated by arrows in Figs. 6(c) and 6(d).

By Dynamic Time Warping (DTW), a distance matrix is generated by calculating the distance from every data point in one signal to each data point in the other signal. The normalized warping distance (WD) is a measure to estimate the cost of aligning two signals, and thus is adopted in thus study to compare signals. The larger the warping distance is, the more difficult
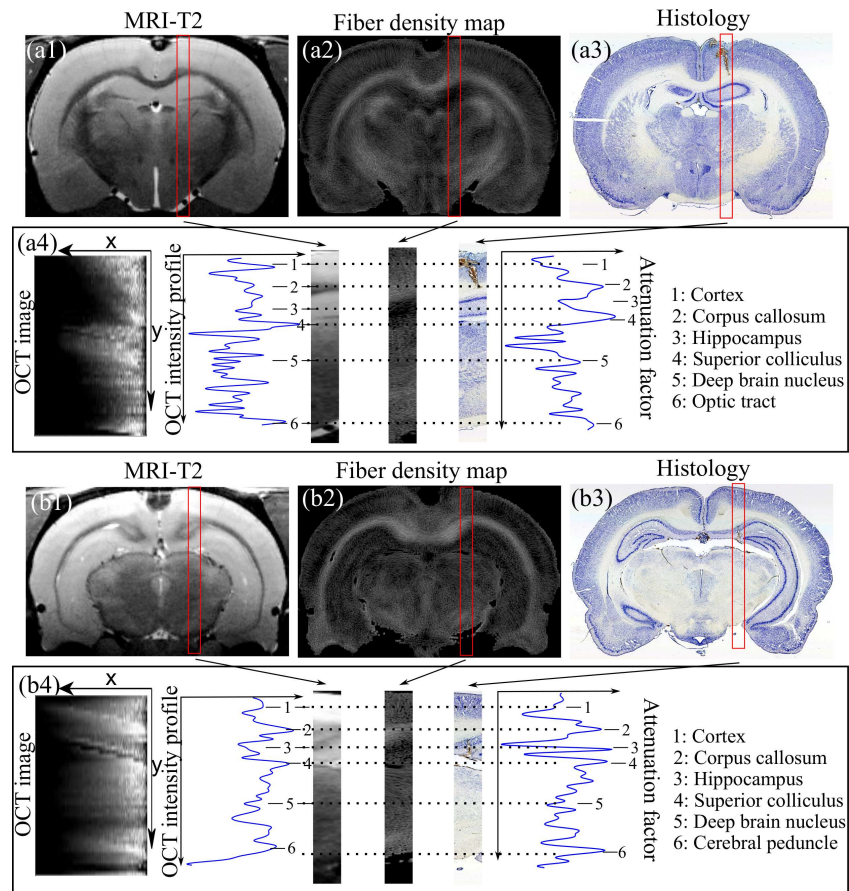
Fig. 4. Two representative illustrations of correlation of anatomical structures between OCT signals, T2-weighted MR image, fiber density map and histology image are shown here. The black dotted lines indicate various identified anatomical structures, and show the agreement between image modalities. Both of the OCT intensity profiles and the attenuation present prominent hyperreflective bands corresponding to corpus callosum, superior colliculus, optic tracts, and as well as cerebral peduncle which are brain white matter basically compose of neural fibers. These structures revealed in OCT images and signals are also distinguishable in MRI and histological images. x, and y axis of OCT images in a4 and b4 denote look ahead distance (mm) and trajectory depth (mm), respectively.
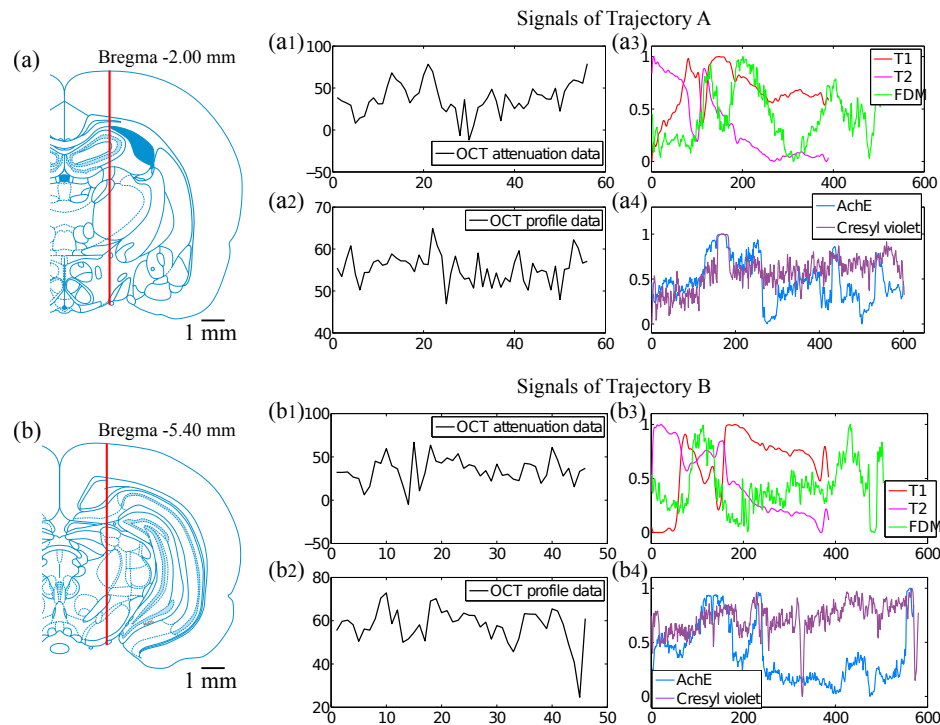
Fig. 5. A collage of OCT data, MRI profiles, and histological profile signals of two sample trajectories. Left panels show the location of trajectories illustrated by the red line in the rat atlas schematics. The coordinate of trajectory A is AP - 2.00 mm, ML - 2.50 mm (a), trajectory B is AP - 5.40 mm, ML - 2.00 mm (b). The plots in right panels are OCT attenuation profile, OCT intensity profile, T1 T2 FDM profile, and histological profile of each trajectory respectively.

it is to warp and align two signals which consequently means that the more distortions of the two signals are corrected. For all six trajectories, we calculated the WD of each compared signal pair and displayed them with box plot shown in Figs. 7(a) and 7(b). Among OCT attenuation data pairs, OCT vs.T2 owned the largest mean WD 17.08 (averaged from 6 trajectories), whereas OCT vs. DTI-FDM had the least mean value of the WD 5.28. OCT vs. T2 had a strong divergent distribution of the WD value, while the WD value of OCT-AChE pair was centralised [Fig. 7(a)]. Among the WD of the OCT profile data pairs, OCT-T2 had the largest WD value of 12.82, while OCT-AChE had the lowest WD value of 5.53 [Fig. 7(b)]. In addition, both OCT-T1 and OCT-T2 featured more a divergent distribution compared with the other signal pairs .

We calculated the correlation coefficient (R) and the mutual information (MI) of the ten signal pairs without applying the DTW process, and presented their distribution with box plot in Figs. 7(c) - 7(f). The R value of all compared signal pairs were lower than 0.5, with 90% of the median R value were lower than 0.2. This finding indicates the OCT signals are not linearly correlated to other modalities under the validation method of correlation coefficient. While the mutual information of OCT against MRI, including both T1-weighted and T2-weighted images, were markedly greater than the other signal pairs, as shown in Figs. 7(e) and 7(f).
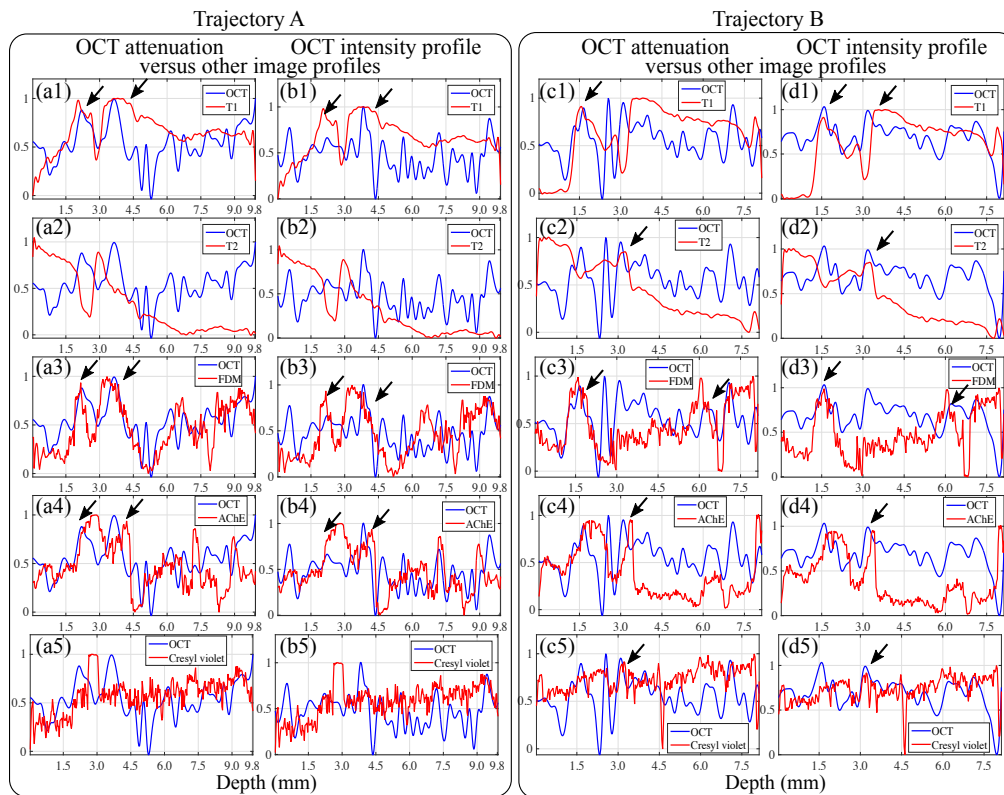
Fig. 6. OCT measurements including intensity profile and attenuation factor of trajectory A and B align with intensity profiles of MR-T1, MR-T2, FDM, AChE staining profile, and cresyl violet staining profile. Resemblances are indicated by arrows.

4. Discussion

4.1. Correlation ratios

In this study, we aimed to give both qualitative and quantitative evaluation of *in vivo* OCT measurement of rat brain by correlating the OCT measurement with other image modalities, such as MRI images and histological images. To accomplish the quantitative evaluation for each measured brain trajectory we extracted two quantitative signals from OCT measurements: (i) tissue attenuation factor as a function of the trajectory depth, (ii) profile of the reconstructed OCT grayscale intensities along the trajectory. Warping distance (WD) elicited from dynamic time warping, correlation coefficient (R) and mutual information (MI), were the measures selected in this study to estimate the correlation ratios of two compared cross-modality signals.

OCT versus MRI

When correlating the OCT attenuation profile with the profile data of T1 and T2-weighted MR images, it required more computing cost (larger warping distance) obtain an optimal alignment in the DTW process. In addition, the compared signal pairs also had low correlation coefficient values meaning they have weakly linear correlation. This is presumably induced by the difference in the essential imaging principle of OCT and MRI. In MRI, the contrast between tissue types is based on the differences in the spin relaxation rate and density of hydrogen atoms. T1 and T2 decay constants are fundamental properties of biological tissue containing water molecules. In brain tissue, cerebrospinal fluid (CSF) has the longest T1 and T2, gray matter has
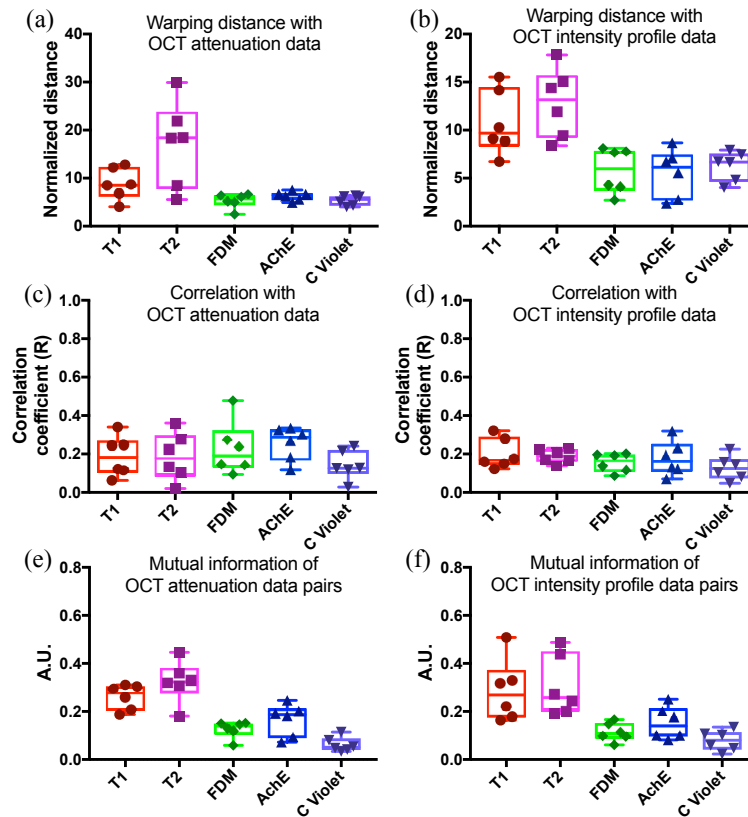
Fig. 7. The upper two figures are warping distance distribution depicted with box plot. The middle and lower rows of figures are the distribution of correlation coefficient (R) and mutual information (MI) of the compared signal pairs before warping process, respectively.

a median T1 and T2, and white matter has the shortest time [33]. The signal intensity of each tissue type in MRI images eminently corresponds to its relaxation time and hydrogen density. Compared with optical properties, the ratio of these values do not strongly change in subclasses of anatomical structures, like the thalamus and cortex. This yields to a low contrast in MRI between gray matter structures [34, 35]. However, among the five different imaging modalities we used to compare with OCT measurements, the mutual information of MRI versus OCT were markedly higher than the others. Presumably, this results from a lower joint entropy meaning there are more shared information within these two modalities irrespective to linear relation.

OCT versus fiber density maps (FDM)

The contrast within fiber density map (FDM), which is derived from DTI and fiber tractography, represents the best estimation of the degree of the water molecule's diffusion at that position presumably along fibrous structures. In neuroimaging, DTI is often employed to depict white matter tracts and thus brain connectivity with mapping of the axonal connections. Whereas, the lipid-rich myelin sheaths of axons or axons bundles feature with a high scattering property which thus gives high backscattering intensity in OCT signals [36]. Although we expected the OCT and fiber density map which is derived from the DTI acquisition may feature the highest correlation since they have very similar origin of contrast, the three different statistical correlation measures we estimated did not present any significant higher correlations than the other modalities. Nevertheless, resemblances and overlaps which are corresponding to some identified anatomical structures including corpus callosum, superior colliculus and etc., were

determined between OCT and FDM profile signals and are shown in Fig. 6.

OCT versus histology

In other studies, OCT cross-sectional images are often evaluated by comparing with the corresponding histology images [37]. Here, we assessed the OCT A-scan signals with the corresponding histological profile signals. In cresyl violet staining, cell core and Nissl substance appear in dark violet colour, whereas cytoplasm and the rest substance appear in light violet or light blue [38]. Thus, the brain region where cell density is higher such as cortex and dentate gyrus layer in hippocampus, features a low gray scale intensity value in the profile signal. On the contrary, white matter consists of lipid-rich myelinated fibers has a high gray scale intensity value. AChE staining is used to determine the distribution of acetylcholinesterase (AChE) in brain sections, the intensity of which is an indication of the quantity of the enzyme present which correspond to the distribution of the neurotransmitter acetylcholine (ACh) [38, 39]. Axon fiber possessing low quantity of ACh has extremely high gray scale intensity in the profile signal, while gray matter containing predominantly neuron cell bodies appears darker in the image featuring low intensity value of the profile signal. Noticeably, AchE better correlates to OCT signal featuring a higher correlation coefficient and mutual information, compared to c-violet staining.

4.2. Methodology and limitations

In neurosurgery, minimally-invasive intervention is much appreciated as it leads to minimal tissue disruptions and less complications compared to open craniotomy [40, 41]. Such a procedure is often adopted in deep brain stimulation [42] and epilepsy surgery [43], where recording microelectrodes are implanted into deep brain structures. Fiber-based endoscopic imaging modalities, including optical coherence tomography [9], optical diffuse reflectance spectroscopy [44] and others, have been developed to guide the implantation. The guidance is realized by identifying tissue type in the vicinity of the electrode for localization, and most crucially by visualizing tissue ahead of the electrode to avoid penetrating any critical structures such as major vessels. To facilitate *in vivo* OCT measurement of deep brain structures, a particularly thin fiber probe, which can be easily fitted into the working channel of any existing neuronavigation tools or/and integrated with the electrode, is desired. We are aware that a rotating probe utilized in intracoronary OCT could provide informative cross-sectional images of the surrounding tissue, however for the specific neurosurgery guidance forward imaging modality is still preferred as it reveals particularly what is ahead of the probe. As such, there is certainly a need to evaluate the 1-D OCT measurement from forward scanning and compare to the other imaging modality.

We are aware that there are various factors which could affect the quantification such as the focal length and sensitivity variations with wavelength [45, 46]. The quantitative tissue attenuation coefficient can be estimated to characterize tissue types when OCT A-scans are calibrated with known reflectance from a glass/air interface and corrected with uniform diffuse-scattering media [47, 48]. In our work, A-scan amplitude was calibrated and normalized to a glass/air interface, however it was not corrected with a homogeneous optical phantom. Thus we are fully conscious that the attenuation coefficient we extracted from OCT A-scans are not directly comparable with measurements from other systems. Nevertheless, the tissue attenuation factors (instead of using the term of "attenuation coefficient") we determined are able to differentiate brain tissue types in this study.

Contrast in OCT data sets originates in tissue's optical scattering properties at the illuminating wavelength. Therefore, the OCT attenuation profile reflects the tissue attenuation coefficient (sum of scattering coefficient and absorption coefficient) distribution along the trajectory, whilst the OCT intensity profile reveals the tissue reflectivity (backscattering property) along the trajectory. Aim of this study was to take a step towards a better understanding of the OCT contrast in vivo. However, it goes far beyond the scope of this study to take differences in optical prop-

erties on a cellular scale, like geometrical features as structures perpendicular to the light path as opposed to parallel paths, round fibers vs. ill-defined somata, as well as specific optical properties, like dichroic myelin sheaths as opposed to simple neuron membranes, to name a few, into account. Still, above mentioned measurements enabled us to conservatively compare OCT contrast to other imaging modalities.

5.   Conclusion

In this study we report, to our best knowledge, the first quantitative evaluation of the *in vivo* OCT measurement of rat brain by correlating them with the corresponding MRI signals and histological signals. We evaluated in total ten signal pairs which were OCT attenuation profile versus T1 and T2-weighted MR images, fiber density maps (FDM), Histo-AChE, and Histo-CViolet respectively, and OCT intensity profile versus T1 and T2-weighted MR images, fiber density maps, Histo-AChE, and Histo-CViolet respectively. We estimated the degree of the correlation of the compared signal pair by determining warping distance (WD), statistics correlation coefficient (R) and mutual information (MI). We found that the OCT measurements shared more information with MRI images with notably higher mutual information values. The OCT measurements had relevant correlation with both AChE and cresyl violet staining. Since the contrast in all three well correlating imaging modalities (FDM, CV and AChE) is based on fibrous, little cell containing structures, we primarily conclude, that OCT image contrast in brain is strongly linked to the appearance of the very same fibrous, well ordered and myelin-rich structures. This quantitatively supported conclusion backs up our previously proposed minimally invasive, endoscopic in vivo brain imaging method [9], but casts doubt on the usability of OCT to online monitor gliotic ensheathing of brain implants [11].

Funding